Schwinger-boson mean-field study of the spin-1/2 J_1-J_2-J_χ model in the honeycomb lattice: Thermal Hall signature

Rohit Mukherjee, Ritajit Kundu, Avinash Singh, and Arijit Kundu *
Department of Physics, Indian Institute of Technology—Kanpur, Kanpur 208 016, India

(Received 24 April 2022; revised 30 January 2023; accepted 31 March 2023; published 11 April 2023)

We theoretically investigate, within Schwinger-boson mean-field theory, the transition from a gapped $\mathbb{Z}_2$ quantum spin liquid, in a J_1-J_2 Heisenberg spin-$\frac{1}{2}$ system in a honeycomb lattice, to a chiral $\mathbb{Z}_2$ spin-liquid phase under the presence of time-reversal symmetry-breaking scalar chiral interaction (with amplitude J_χ). We numerically obtain a phase diagram of this J_1-J_2-J_χ system, where different ground states are distinguished based on the gap and the nature of excitation spectrum, topological invariant of the excitations, the nature of spin-spin correlation, and the symmetries of the mean-field parameters. The chiral $\mathbb{Z}_2$ state is characterized by the nontrivial Chern number of the excitation bands and lack of long-range magnetic order, which leads to a large thermal Hall coefficient.

DOI: 10.1103/PhysRevB.107.155122

I. INTRODUCTION

Quantum spin liquid (QSL) is an exotic state of matter where a spin system does not develop magnetic order or break any lattice symmetry even at the absolute zero temperature. Instead, the system develops a topological order with fractionalized excitations [1–3]. QSLs cannot be described by the traditional Landau paradigm where different phases are characterized by local order parameters and broken symmetry. Historically, QSL was proposed by Anderson [4] as a quantum ground state for a geometrically frustrated triangular lattice antiferromagnet, and since then, the search for QSL in quantum magnets has primarily focused on frustrated lattice systems, such as triangular, kagome, and pyrochlore lattices. Among possible candidates, the Kitaev model for spin-$\frac{1}{2}$ on a honeycomb lattice is a promising candidate to support QSL states, where strong quantum fluctuations arising from the bond-dependent interaction destroys magnetic orders [3,5,6]. This led to an intense experimental search for Kitaev materials and signatures of the QSL state [7,8]. In addition to Kitaev's honeycomb model, the antiferromagnetic Heisenberg J_1-J_2 model has been studied extensively as a possible QSL candidate [9,10]. The conventional ground state of the nearest-neighbor Heisenberg model (without the next-nearest-neighbor coupling J_2), say, on the honeycomb lattice, is a Néel ordered state, but when the second-nearest interaction is turned on and increased, the long-range order can get destroyed, and the system can enter into a quantum disordered state for the intermediate coupling regime. Authors of various numerical studies suggest that there is a QSL phase for an intermediate ratio of J_2/J_1, although the parameter range of the regime has been somewhat debated [11–18]. Apart from the physics associated with QSLs, they also hold potential for applications, especially in the field of quantum information processing [19], using properties of the long-range entangled spins. For example, the Kitaev QSL can support fractional excitations, represented by Majorana fermions [8], which can be made to act as anyons obeying non-Abelian statistics. Braiding these anyons could be an important step toward topological quantum computation [2].

In recent years, there have also been numerous studies to identify chiral spin orders in disordered systems, such as the scaler chiral order [i.e., $\langle \vec{S}_i \cdot (\vec{S}_j \times \vec{S}_k) \rangle \neq 0$, where $\vec{S}_i$ is the spin-operator at the ith site]. The presence of such time-reversal (TR) symmetry-breaking chiral order can give rise to nonzero Chern numbers of the excitations, which can result in enhanced thermal Hall conductivity. In certain cases, these states can be identified as chiral spin liquids (CSLs), based on their ground-state degeneracy, which have been also studied extensively in kagome [20–26], triangular [27–30], square [31], and honeycomb lattices [32]. Very recently, authors of Ref. [33] have investigated the topological phase transition and nontrivial thermal Hall signatures for spins in a honeycomb lattice in the presence of Zeeman coupling using Abrikosov-fermion mean-field theory; they also report similar findings of an unusual thermal Hall effect for the pseudogap phase of copper-based superconductors [34].

In this paper, we consider the J_1-J_2 spin-$\frac{1}{2}$ Heisenberg model along with a scalar chiral three-spin term. Without the scalar chiral term, in the classical limit $S \to \infty$, the system is Néel ordered for $J_2/J_1 < \frac{1}{6}$ and magnetically ordered in a spiral manner for $J_2/J_1 > \frac{1}{6}$ [35–37]. For the quantum case, the nature of the ground state has been extensively studied (without the scalar chiral term), using spin-wave theory [36–39], the nonlinear σ model [40], exact diagonalization [15,41], variational Monte Carlo [11,18], and other methods [42]. The general understanding is that, for $J_2/J_1 \lessapprox 0.21$, it orders magnetically as a Néel phase; in the range $0.37 \lessapprox J_2/J_1 \gtrapprox 0.21$, there is a gapped spin-liquid (GSL) phase; in the range $0.4 \lessapprox J_2/J_1 \gtrapprox 0.37$, there is a C_3-rotational symmetry-broken

* arijit.hri@gmail.com

disordered valence-bond crystal (VBC) state, and for $J_2/J_1 \gtrapprox 0.4$, the system orders magnetically in a spiral manner.

Our work is based on Schwinger-boson mean-field theory (SBMFT), where we find that the introduction of a scalar spin-chiral term on the disordered (gapped) phase leads to transition to chiral $\mathbb{Z}_2$ spin-liquid (CZSL) states, where the Chern numbers of the excitation bands change. We also theoretically study its signature in the thermal Hall measurement, which captures the nontrivial topology of the spinon bands.

Before we present details of the study, we note that there are two approaches which are widely used in the literature to investigate spin-liquid phases: Schwinger/Abrikosov-fermion mean-field theory [43,44] and SBMFT [45–47], in which the low-energy spin excitations are fermionic and bosonic, respectively. The fermionic approach is more suited to explain the physics near a continuous Mott transition [48–50], and the bosonic approach is more suitable near magnetic phase transitions. At the spin-liquid–to–magnetically ordered state transition, the gap vanishes at particular momentum points in the Brillouin zone where the bosonic spinons can condensate, giving rise to magnetic ordering. The advantage of the Schwinger-boson approach lies in the fact that we can access both the spin-liquid states and the magnetically ordered state.

This paper is organized as follows. In Sec. II, we briefly review the formalism of SBMFT and various technicalities involved in solving for the ground-state properties. We provide details of the numerical simulation and further discussion of how we identify various phases from numerical data in Sec. III, and we present the numerical results in Sec. IV. We discuss the results further and summarize our findings in Sec. V.

II. FORMALISM

In this paper, we study the effect of the scaler three-spin chiral term, with coefficient J_χ, in the J_1-J_2 Heisenberg spin-$\frac{1}{2}$ Hamiltonian:

$$H = \sum_{nn} J_1 \vec{S}_i \cdot \vec{S}_j + \sum_{nnn} J_2 \vec{S}_i \cdot \vec{S}_j + \sum_{\triangle} J_\chi \vec{S}_i \cdot (\vec{S}_j \times \vec{S}_k), \quad (1)$$

where $\vec{S}_i$ is the spin operator at site i, J_1 and J_2 are the coupling amplitudes for the nearest neighbor (abbreviated as *nn*) and the next-nearest neighbors (abbreviated as *nnn*), whereas J_χ is the amplitude of the scalar spin-chiral term, as outlined in the Fig. 1. In the third term, the sum involves the triangular plaquettes Δ formed by the nearest neighbors, as shown in the same figure.

As a passing comment, strong coupling expansion of the Hubbard model yields $J_1 = 4t_1^2/U$ and $J_2 = 4t_2^2/U$, where t_1 and t_2 are the nearest- and next-nearest-neighbor hopping amplitudes of electrons, respectively, and U is the on-site repulsion. On the other hand, scalar spin chirality is proportional to $-24t_1^2 t_2/U^2 \sin\Phi$, where Φ is the magnetic flux through the triangular plaquette [51]. Starting from the Haldane-Hubbard model, one may also naturally lead to the J_χ term without any further application of magnetic field [21,32,32,51–54]

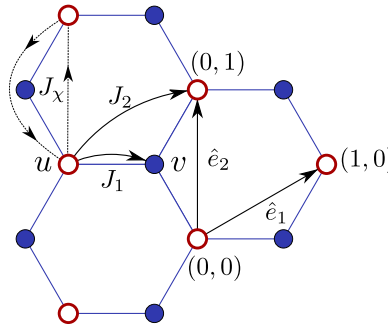

FIG. 1. Honeycomb lattice is defined by translation vectors ($\hat{e}_1$,$\hat{e}_2$) and two sublattices u and v. The spin-spin exchange couplings up to second order (J_1 and J_2, respectively) and the chiral coupling J_χ are depicted.

We study this spin model, Eq. (1), using SBMFT, where we represent the spin operators in terms of bosons. The nature of the bosonic excitations on top of the mean-field ground state predicts order-disorder transition and other physical properties of the system, as we discuss later. Before we discuss our numerical findings, we present a short review of SBMFT below.

A. SBMFT

The principle idea behind SBMFT is to express the spin operators in terms of bosonic operators that carry spin. In the SU(2) representation, where two bosonic flavors are introduced to describe the spin operators, we write [55]

$$\vec{S}_i = \tfrac{1}{2} b^\dagger_{i,\sigma} \vec{\tau}_{\sigma\sigma'} b_{i,\sigma'}, \quad (2)$$

where τ^i are the Pauli matrices, and $b^\dagger_{i,\sigma}$ are the bosonic creation operator of spin σ on site i. To preserve the SU(2) commutation rule, the following local constraint must be fulfilled on every site:

$$\sum_\sigma b^\dagger_{i\sigma} b_{i\sigma} = 2S, \quad (3)$$

where S is the value of spin under consideration, which we take to be $\frac{1}{2}$ in this paper. However, it is typically difficult to impose this constraint exactly [46]; thus, we impose it on the average over the mean-field ground state, which is the most common practice in the literature.

As we do not impose any symmetry to be broken in the ground state, the only possible bilinears that preserve the spin-rotation symmetry are the following:

$$\hat{A}_{ij} = \tfrac{1}{2}[b_{i\uparrow} b_{j\downarrow} - b_{i\downarrow} b_{j\uparrow}],$$
$$\hat{B}_{ij} = \tfrac{1}{2}[b^\dagger_{i\uparrow} b_{j\uparrow} + b^\dagger_{i\downarrow} b_{j\downarrow}]. \quad (4)$$

Physically, A_{ij}'s measure singlet-type correlations, while B_{ij}'s measure triplet correlations [56]. In a gapped phase, the first one is favored, whereas the triplet correlation allows the spinons to hop between sites, giving rise to long-range orders.

It can be easily verified that

$$\vec{S}_i \cdot \vec{S}_j =: \hat{B}^\dagger_{ij} \hat{B}_{ij} : - \hat{A}^\dagger_{ij} \hat{A}_{ij}, \quad (5)$$

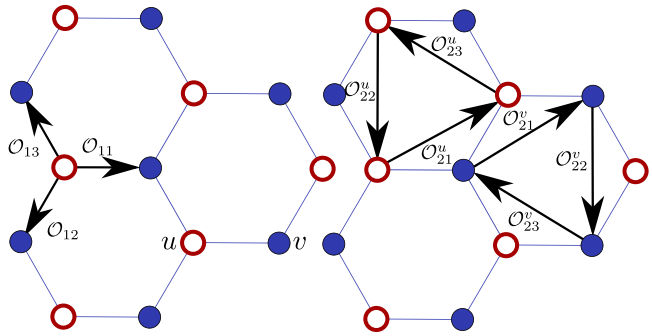

FIG. 2. The nine independent mean-field complex parameters O_{id} and their clockwise orientation conventions that allow the point group symmetry breaking. The first subscript i refers to the neighbors ($i = 1, 2$ for the nearest and the next nearest, respectively), while the second subscript d refers to the three directions. For the next-nearest neighbors $i = 2$, connected sites are on the same sublattices; we then introduce two sets of mean-field parameters, labeled with the extra superscript O^w, with $w = u/v$. O can be of type A or B between the sites, totaling 18 independent parameters.

where $:\hat{O}:$ refers to the normal ordering. Now, we perform the mean-field decoupling of $\hat{A}$, $\hat{B}$ operators as

$$\begin{aligned}\hat{A}^\dagger_{ij}\hat{A}_{ij} &\to A^*_{ij}\hat{A}_{ij} + \hat{A}^\dagger_{ij}A_{ij} - A^*_{ij}A_{ij},\\ \hat{B}^\dagger_{ij}\hat{B}_{ij} &\to B^*_{ij}\hat{B}_{ij} + \hat{B}^\dagger_{ij}B_{ij} - B^*_{ij}B_{ij},\end{aligned} \tag{6}$$

where A, B are the complex-valued mean-field order parameters that one computes self-consistently from the average over the mean-field ground state $|\mathrm{gs}\rangle$:

$$A_{ij} = \langle \mathrm{gs}|\hat{A}_{ij}|\mathrm{gs}\rangle\,, \qquad B_{ij} = \langle \mathrm{gs}|\hat{B}_{ij}|\mathrm{gs}\rangle\,. \tag{7}$$

These expectation values collectively define the parameters of the mean-field *Ansatz*. The expectation values are calculated in the new basis that diagonalizes the Hamiltonian, and using

$$\gamma_{\vec{q},\lambda}\,|\mathrm{gs}\rangle = 0, \tag{8}$$

where $|\mathrm{gs}\rangle$ is the vacuum state for the resulting bosonic excitation $\gamma_{\vec{q},\lambda}$, details of these procedures will be discussed in the Sec. II C. Once the decomposition in Eq. (6) is done, the effective mean-field Hamiltonian is completely expressed in terms of the bosonic bilinears. In the same way, we can do the SBMFT decoupling of the scaler chirality term where we use the following identity:

$$\begin{aligned}\vec{S}_i\cdot(\vec{S}_j\times\vec{S}_k) &= 2i(-\hat{B}^\dagger_{ki}\hat{B}^\dagger_{jk}\hat{B}^\dagger_{ij} + \hat{B}_{ij}\hat{B}_{jk}\hat{B}_{ki}),\\ &= -4\mathrm{Im}[\hat{B}_{ij}\hat{B}_{jk}\hat{B}_{ki}],\end{aligned} \tag{9}$$

which we write using the mean-field decomposition as

$$\begin{aligned}\hat{B}_{ij}\hat{B}_{jk}\hat{B}_{ki} \approx{}& \hat{B}_{ij}\,\langle\hat{B}_{jk}\rangle\,\langle\hat{B}_{ki}\rangle + \langle\hat{B}_{ij}\rangle\,\hat{B}_{jk}\,\langle\hat{B}_{ki}\rangle\\ &+ \langle\hat{B}_{ij}\rangle\,\langle\hat{B}_{jk}\rangle\,\hat{B}_{ki} - 2\,\langle\hat{B}_{ij}\rangle\,\langle\hat{B}_{jk}\rangle\,\langle\hat{B}_{ki}\rangle\,.\end{aligned} \tag{10}$$

In our original Hamiltonian, we have the Heisenberg interactions up to second-nearest neighbor. Now, if we want to preserve the translational symmetry but break all the point group symmetries, we can get at most 18 inequivalent mean-field *Ansätze* (bond parameters), nine for each A_{ij} and B_{ij}. These are schematically shown in Fig. 2. For nearest-neighbor interactions, the bonds are between one u and one v sublattice, denoted by O_{1d}, where d's are the three possible orientations (subscript 1 denotes nearest neighbor). For the next-nearest interactions, the bonds are connections between two u or v sublattices. We denote them with O^w_{2d}, where the superscript represents the sublattice index and d's are the three possible orientations as before. Each O can be chosen as A or B type of order parameters, totaling 18 of them.

The final mean-field Hamiltonian can be expressed as

$$\begin{aligned}H_{\mathrm{mf}} = {}& \sum_{ij} J_{ij}(-A^*_{ij}\hat{A}_{ij} + B^*_{ij}\hat{B}_{ij} + \mathrm{H.c.})\\ &- \sum_i \mu_i\left(\sum_\sigma b^\dagger_{i\sigma}b_{i\sigma} - 2S\right)\\ &+ 2i\sum_{\triangle} J_\chi\,(B_{ki}B_{jk}\hat{B}_{ij} + B_{ij}B_{ki}\hat{B}_{jk}\\ &+ B_{ij}B_{jk}\hat{B}_{ki} - \mathrm{H.c.}) + K,\end{aligned} \tag{11}$$

with

$$K = \sum_{ij} J_{ij}(|A_{ij}|^2 - |B_{ij}|^2) + 8\sum_{\triangle} J_\chi\,\mathrm{Im}(B_{ij}B_{jk}B_{ki}). \tag{12}$$

The above term in the Hamiltonian is the consequence of the constraint in Eq. (3). Here, the chemical potentials μ_u and μ_v depend on the sublattices. The Schwarz inequality restricts the upper bounds on the moduli $|A| \leqslant S + \frac{1}{2}$, $|B| \leqslant S$, which must be obeyed for any self-consistent *Ansatz* in SBMFT [46].

B. Diagonalization of bosonic quadratic Hamiltonian

The mean-field Hamiltonian, Eq. (11), can be diagonalized using the Bogoliubov-Valantin canonical transformation [57,58]. The procedure is following for a generic quadratic bosonic Hamiltonian:

$$H = \tfrac{1}{2}\Psi^\dagger M\Psi; \qquad \Psi^\dagger = (b^\dagger_1,\ldots,b^\dagger_N,b_1,\ldots,b_N), \tag{13}$$

where N is the degree of freedom and M is an $2N\times 2N$ matrix. Here, $b^\dagger_n$ (b_n) are the creation (annihilation) operators in momentum, spin, or any other degrees of freedom. To find the eigenvectors corresponding to the matrix M, we introduce creation (annihilation) operators $\gamma^\dagger_m$ (γ_m) such that

$$\Psi = T\Gamma, \qquad \Gamma^\dagger = (\gamma^\dagger_1,\ldots\gamma^\dagger_N,\gamma_1,\ldots\gamma_N), \tag{14}$$

where T is the basis-transformation matrix. We choose our T such that the Hamiltonian in Eq. (13) can be written in a diagonal form as

$$H = \tfrac{1}{2}\Gamma^\dagger T^\dagger MT\Gamma, \tag{15}$$

with

$$T^\dagger MT = \begin{pmatrix}\omega_1 & 0 & \cdots & 0\\ 0 & \omega_2 & \cdots & 0\\ \vdots & \vdots & \ddots & \vdots\\ 0 & 0 & \cdots & \omega_{2N}\end{pmatrix}.$$

To preserve the bosonic commutation rules, the Ψ and Γ matrices should obey the following matrix equation:

$$[\Psi_i,\Psi^\dagger_j] = [\Gamma_i,\Gamma^\dagger_j] = (\rho_3)_{ij},$$

where

$$\rho_3 \equiv \begin{pmatrix} I_{N\times N} & 0 \\ 0 & -I_{N\times N} \end{pmatrix}. \tag{16}$$

Here, $I_{N\times N}$ is the identity matrix of dimension N. This implies that the transformation matrix must satisfy

$$T\rho_3 T^\dagger = \rho_3. \tag{17}$$

In a more formal language, T is a paraunitary [58] SU(N, N) matrix. The elements of the transformation matrix can be found from the eigenvectors of the dynamic matrix, defined as

$$D = \rho_3 M, \tag{18}$$

which satisfies the Heisenberg equation of motion for Ψ [34]. All the eigenvalues of the dynamic matrix (when it is diagonalizable) appear in pairs of opposite signs and are real. Here, T is also referred to as the derivative matrix, consisting of all the eigenvectors of D sorted in the form:

$$T = [V(\omega_1), \ldots, V(\omega_N), V(-\omega_1), \ldots, V(-\omega_N)], \tag{19}$$

with the eigenvectors normalized as

$$V^\dagger(\omega_i)\rho_3 V(\omega_i) = 1, \qquad V^\dagger(-\omega_i)\rho_3 V(-\omega_i) = -1, \tag{20}$$

for all the sets of $[V(\omega_i), V(-\omega_i)]$. After the diagonalization, we have

$$T^{-1}DT = \text{diag}\,(\omega_1, \ldots, \omega_N, -\omega_1, \ldots, -\omega_N), \tag{21}$$

and

$$T^\dagger M T = \text{diag}\,(\omega_1, \ldots, \omega_N, \omega_1, \ldots, \omega_N). \tag{22}$$

Both M and D are now simultaneously diagonalized. We call the positive (negative) bands with indices $n = 1, \ldots, N$ ($n = N+1, \ldots, 2N$) as the particle (hole) bands.

C. Mean-field dispersion

We use the method of the preceding section for diagonalization of the mean-field Hamiltonian in Eq. (11) in the momentum space. We write the bosonic annihilation operator in the Fourier space as

$$b_{\vec{r},w,\sigma} = \frac{1}{\sqrt{n_c}} \sum_{\vec{q}} \exp(i\vec{q}\cdot\vec{r}) b_{\vec{q},w,\sigma}, \tag{23}$$

where n_c is the total number of unit cells in the real-space lattice (each containing two sublattices); $\vec{r}$ are the positions of the unit cells, and $w = u, v$ are sublattice indices. The combination $(\vec{r}, w)$ defines the position of a particular site, and $\sigma = \uparrow / \downarrow$ are the flavors of the Schwinger bosons. Then the mean-field Hamiltonian in the momentum space is written as

$$H_{\text{mf}} = \frac{1}{2}\sum_{\vec{q}} \Psi^\dagger_{\vec{q}} M_{\vec{q}} \Psi_{\vec{q}} - (2S+1)n_c \sum_w \mu_w + K, \tag{24}$$

with

$$\Psi^\dagger_{\vec{q}} = (b^\dagger_{\vec{q},u,\uparrow} b^\dagger_{\vec{q},v,\uparrow} b_{-\vec{q},u,\downarrow} b_{-\vec{q},v,\downarrow}), \tag{25}$$

where the coefficient matrix $M_{\vec{q}} = M^{(1)}_{\vec{q}} + M^{(2)}_{\vec{q}}$ consists of two parts, where the second term is proportional to the scalar chirality J_χ. The first of these terms is given by

$$M^{(1)}_{\vec{q}} = \begin{bmatrix} J_2\left(B^u_{2d}\phi_{2d} + B^{u*}_{2d}\phi^*_{2d}\right) + 2\mu_u & J_1 B^*_{1d}\phi^*_{1d} & J_2 A^u_{2d}(\phi_{2d} - \phi^*_{2d}) & -J_1 A_{1d}\phi^*_{1d} \\ J_1 B_{1d}\phi_{1d} & J_2\left(B^v_{2d}\phi_{2d} + B^{v*}_{2d}\phi^*_{2d}\right) + 2\mu_v & J_1 A_{1d}\phi_{1d} & J_2 A^v_{2d}(\phi_{2d} - \phi^*_{2d}) \\ J_2 A^{u*}_{2d}(-\phi_{2d} + \phi^*_{2d}) & J_1 A^*_{1d}\phi^*_{1d} & J_2\left(B^u_{2d}\phi^*_{2d} + B^{u*}_{2d}\phi_{2d}\right) + 2\mu_u & J_1 B_{1d}\phi^*_{1d} \\ -J_1 A^*_{1d}\phi_{1d} & J_2 A^{v*}_{2d}(-\phi_{2d} + \phi^*_{2d}) & J_1 B^*_{1d}\phi_{1d} & J_2\left(B^v_{2d}\phi^*_{2d} + B^{v*}_{2d}\phi_{2d}\right) + 2\mu_v \end{bmatrix},$$

where we have assumed the summation over repeated index d and $\phi_{id}(\vec{q}) = \exp(i\vec{q}\cdot\vec{\delta}_{i,d})$ is the phase factor associated with the hopping to neighboring sites at distance $\vec{\delta}_{i,d}$ to the ith neighbors ($i = 1$ and 2 refer to nearest and next-nearest neighbors) and in one of three directions d, shown in Fig. 2. The coefficient matrix $M^{(2)}_{\vec{q}}$ is given by

$$M^{(2)}_{\vec{q}} = 2J_\chi \begin{bmatrix} -2\text{Im}C_{11} & C_{12} & 0 & 0 \\ C^*_{12} & -2\text{Im}C_{22} & 0 & 0 \\ 0 & 0 & -2\text{Im}C_{33} & C_{34} \\ 0 & 0 & C^*_{34} & -2\text{Im}C_{44} \end{bmatrix},$$

where C_{ij} are $\vec{q}$-dependent expressions given by

$$\begin{aligned} C_{11} &= B^*_{12}B_{13}\exp(-iq_2) + B^*_{12}B_{11}\exp(-iq_1) \\ &\quad + B^*_{11}B_{13}\exp[i(q_1 - q_2)], \\ C_{22} &= B^*_{13}B_{11}\exp[i(q_2 - q_1)] + B^*_{11}B_{12}\exp(iq_1) \\ &\quad + B^*_{12}B_{13}\exp(-iq_2), \end{aligned}$$

where C_{33} and C_{44} are the same as C_{11} and C_{22}, respectively, after the exchange of $q_1 \to -q_1$ and $q_2 \to -q_2$, and

$$\begin{aligned} C_{12} &= i\{\mathcal{A} - \exp(-iq_1)\mathcal{B} + \exp[-i(q_1 - q_2)]\mathcal{C}\}, \\ C_{34} &= i\{-\mathcal{A}^* + \exp(-iq_1)\mathcal{B}^* - \exp[-i(q_1 - q_2)]\mathcal{C}^*\}. \end{aligned}$$

with

$$\begin{aligned} \mathcal{A} &= B^*_{12}B^{u*}_{21} - B^u_{23}B^*_{13} + B^v_{23}B^*_{13} - B^*_{12}B^{v*}_{21}, \\ \mathcal{B} &= B^{u*}_{22}B^*_{13} + B^u_{21}B^*_{11} + B^*_{13}B^{v*}_{22} - B^v_{21}B^*_{11}, \\ \mathcal{C} &= B^*_{12}B^u_{22} + B^*_{11}B^{u*}_{23} - B^*_{11}B^{v*}_{23} + B^v_{22}B^*_{12}. \end{aligned}$$

To find the eigenmodes corresponding to M, we introduce new annihilation (creation) operators γ ($\gamma^\dagger$), as before, such that

$$\Psi_{\vec{q}} = T_{\vec{q}}\Gamma_{\vec{q}}, \tag{26}$$

with

$$\Gamma^\dagger_{\vec{q}} = (\gamma^\dagger_{\vec{q},u,\uparrow}\gamma^\dagger_{\vec{q},v,\uparrow}\gamma_{-\vec{q},u,\downarrow}\gamma_{-\vec{q},v,\downarrow}). \tag{27}$$

Now the mean-field Hamiltonian takes the form, in this new basis:

$$H_{\rm mf} = \frac{1}{2}\sum_{\vec{q}} \Gamma^{\dagger}_{\vec{q}}\, \hat{\omega}_{\vec{q}}\, \Gamma_{\vec{q}} - (2S+1)n_c \sum_{w} \mu_w + K. \tag{28}$$

The matrix $T_{\vec{q}}$ satisfies the following conditions:

$$T^{\dagger}_{\vec{q}}\, \rho_3\, T_{\vec{q}} = \rho_3, \tag{29}$$

$$T^{\dagger}_{\vec{q}}\, M_{\vec{q}}\, T_{\vec{q}} = \hat{\omega}_{\vec{q}}, \tag{30}$$

where

$$\hat{\omega}_q = I_{2\times 2} \otimes \begin{bmatrix} \epsilon_{\vec{q},u} & 0 \\ 0 & \epsilon_{\vec{q},v} \end{bmatrix}. \tag{31}$$

Now that we have found the mean-field spinon dispersion, one can find the fixed point in the mean-field parameter space by minimizing the free energy:

$$\mathcal{F}_{\rm mf} = \sum_{\vec{q},w} \epsilon_{\vec{q},w} - (2S+1)n_c \sum_{w} \mu_w + K, \tag{32}$$

with respect to the mean-field parameters and the chemical potentials:

$$\frac{\partial \mathcal{F}_{MF}}{\partial O_{id}} = 0, \qquad \frac{\partial \mathcal{F}_{MF}}{\partial \mu_w} = 0. \tag{33}$$

These equations can be solved numerically. In a second procedure, which is the one we employ in this paper, we solve for the mean-field order parameters by self-consistently solving Eq. (7). Also, in the latter method, the complex nature of the *Ansätze* is inherent compared with solving them by minimizing the free energy.

D. Spin-structure factor

Although we work in a finite-sized lattice system, how the static spin-structure factor $\langle \vec{S}_0 \cdot \vec{S}_i \rangle$ behaves as a function of R_i reveals the nature of the underlying ground state. In such a finite-sized system, the spin-rotation symmetry is never broken in the ground state, which allows us to write

$$\begin{aligned}\langle \vec{S}_0 \cdot \vec{S}_i \rangle &= 3\langle S^z_0 S^z_i \rangle \\ &= \frac{3}{4}\langle (\hat{b}^{\dagger}_{0\uparrow}\hat{b}_{0\uparrow} - \hat{b}^{\dagger}_{0\downarrow}\hat{b}_{0\downarrow})\,(\hat{b}^{\dagger}_{i\uparrow}\hat{b}_{i\uparrow} - \hat{b}^{\dagger}_{i\downarrow}\hat{b}_{i\downarrow})\rangle. \end{aligned} \tag{34}$$

In the Fourier space, we have

$$\begin{aligned} S^z_0 S^z_i = \frac{1}{4n_c^2} \sum_{\vec{k},\vec{q},\vec{k}',\vec{q}'} & \exp[i(\vec{q}-\vec{q}')\cdot\vec{r}_i] \\ & \times [\hat{b}^{\dagger}_{\vec{k}\uparrow}\hat{b}_{\vec{k}'\uparrow}\hat{b}^{\dagger}_{\vec{q}\uparrow}\hat{b}_{\vec{q}'\uparrow} + \hat{b}^{\dagger}_{\vec{k}\downarrow}\hat{b}_{\vec{k}'\downarrow}\hat{b}^{\dagger}_{\vec{q}\downarrow}\hat{b}_{\vec{q}'\downarrow} \\ & - \hat{b}^{\dagger}_{\vec{k}\uparrow}\hat{b}_{\vec{k}'\uparrow}\hat{b}^{\dagger}_{\vec{q}\downarrow}\hat{b}_{\vec{q}'\downarrow} - \hat{b}^{\dagger}_{\vec{k}\downarrow}\hat{b}_{\vec{k}'\downarrow}\hat{b}^{\dagger}_{\vec{q}\uparrow}\hat{b}_{\vec{q}'\uparrow}], \end{aligned} \tag{35}$$

where we have suppressed the sublattice index for brevity. The expectation values of these operators can be calculated in the diagonal basis of the Hamiltonian and using Eq. (8) [59].

E. Berry curvature and thermal Hall effect

Once we diagonalize the bosonic Hamiltonian, we have the Hamiltonian of the excitation in the form of

$$H^{\rm D} = \sum_{\vec{q}} \sum_{n=1}^{N_{\rm band}} \epsilon_{\vec{q},n}\left(\gamma^{\dagger}_{\vec{q},n}\gamma_{\vec{q},n} + \frac{1}{2}\right), \tag{36}$$

where $N_{\rm band}$ is the number of bosonic particle bands (with $\epsilon_{\vec{q},n} > 0$), which is two in our case. The thermal Hall coefficient for this bosonic system is then defined as [60]

$$\kappa_{xy} = -\frac{k_B^2 T}{\hbar V}\sum_{\vec{q}}\sum_{n=1}^{N_{\rm band}}\left\{c_2[n_B(\epsilon_{\vec{q},n})] - \frac{\pi^2}{3}\right\}\Omega_{n\vec{q}}, \tag{37}$$

where $n_B(\omega)$ is the Bose distribution function,

$$c_2(x) = \int_0^x dt \left(\ln\frac{1+t}{t}\right)^2, \tag{38}$$

and $\Omega_{n\vec{q}}$ is the Berry curvature in momentum space for the nth band, defined as

$$\Omega_{n\vec{q}} \equiv i\epsilon_{\mu\nu}\left[\rho_3 \frac{\partial\, T^{\dagger}_{\vec{q}}}{\partial k_\mu}\rho_3 \frac{\partial T_{\vec{q}}}{\partial k_\nu}\right]_{nn}, \tag{39}$$

which can also be recast in the following form:

$$\Omega_{n\vec{q}} = i\epsilon_{\mu\nu}\,\langle \partial_\mu \psi_n(q)|\,\rho_3\,|\partial_\nu\psi_n(q)\rangle\,, \tag{40}$$

where $\psi_n(k)$ is the nth column of the T_q matrix. The numerical evaluation of the Berry curvature follows the U(1)-link variable method, outlined in Appendix A. The Chern number is then evaluated as

$$C_n = \frac{1}{2\pi}\int_{BZ} \Omega_{n\vec{q}}\, d\vec{q}, \tag{41}$$

which are always integers and obey the following constraints:

$$\sum_{n=1}^{N_{\rm band}} C_n = \sum_{n=N_{\rm band}+1}^{2N} C_n = 0, \tag{42}$$

that is, the sums of Chern numbers over particle and hole bands are individually zero [60].

III. DETAILS OF THE NUMERICAL SIMULATION

We solve for self-consistent values of the mean-field parameters in a finite lattice of $n_c = N_s \times N_s$ unit cells, where $N_s = 36$, in total containing $2 \times 36 \times 36$ sites, considering the two sublattices. There is a numerical advantage in solving self-consistently Eq. (7) rather than solving Eq. (32), as it requires no evaluation of numerical derivatives, which can introduce errors of the order of grid separation ($\sim 1/N_s$) and allows for finding completely unrestricted solutions [56]. We take $J_1 = 1$ as our unit of energy and the distance between two neighboring u sublattices as our unit of length.

The minimization technique we use is as follows. First, we choose a set of mean-field parameters O depending on the possible ground state, which needs to be chosen carefully for convergence. In the initial step, for this set of O's, we scan for allowed values of the chemical potentials μ_u, μ_v such that the constraint, Eq. (3), is satisfied on both sublattices in the

ground state average. In the next step, we evaluate the modified mean-field parameters using Eq. (7) [which is simplified by using Eq. (8)], and again, we find appropriate μ_u, μ_v such that the constraint, Eq. (3), is satisfied on both sublattices in the modified ground state. This procedure continues until the mean-field parameters as well as the chemical potentials converge up to a value of tolerance. We first obtain the solutions for $J_\chi = 0$, and then we use these solutions as initial seeds for solutions with small J_χ and follow the same procedure with successively increasing J_χ. In our case, the tolerance on mean-field parameters is at least $\sim 10^{-6}$. The values of the converged mean-field *Ansätze* are all real for a topologically trivial phase, but following the phase transition to a topologically nontrivial phase, some of them acquire complex values. Because we are dealing with spin-half systems, we must always preserve $|A| \leqslant 1$ and $|B| \leqslant 0.5$, which is constrained by the Schwarz inequality; the final converged solutions must also reflect this.

Physically, A_{ij}'s measure singlet-type correlations, while the B_{ij}'s measure triplet correlations [56]; so while choosing the initial values of the mean-field order parameters in the ordered state, B_{ij} should be kept large, while in the disordered state, it should be kept small to get quick convergence.

We distinguish different phases of the ground state by following properties. First, we call a state gapless, if the gap in the spectrum is $< 1/N_s$, as there is always a finite-sized gap present in our system, even though the state can be gapless in the thermodynamic limit. Next, we look for the symmetries of the converged mean-field parameters, which can predict the nature of the ground state based on projective symmetry ground analysis, which we present later. In the gapless state, the momentum where the spectrum is minimum dictates the ordering vector and thus the nature of the long-range order. For the gapped state, we also compute the Chern number of one of the excitation bands to distinguish between a trivial QSL state (we call it GSL) or VBC, where the Chern number is zero, from a CZSL state (with nonzero Chern number). Finally, we also compute the static spin-spin correlation in the ground state. How fast this correlation decays as a function of the distance between two sites can differentiate the nature of the ground state.

1. Projective symmetry of Ansatz

The idea of projective symmetry group (PSG) classification for spin liquids was introduced by Wen [44,61] and Zhou and Wen [62], in the context of the Schwinger-fermion approach. PSG analysis in the Schwinger-boson approach was extended by Wang and Vishwanath [46]. The study of PSGs provides the allowed symmetries and sign structures of the mean-field *Ansatz*. In the disordered phase, we want our mean-field state to obey the underlying microscopic symmetries of the spin model. For a honeycomb lattice, these symmetry transformations are lattice translations, point group symmetries (i.e., C_3 rotation and reflections), spin-rotation symmetry, and the TR symmetry. Additionally, for the case of Schwinger bosons, under the local U(1) transformation:

$$b_{\vec{r}\sigma} \rightarrow \exp[i\phi(\vec{r})] b_{\vec{r}\sigma}, \tag{43}$$

the mean-field *Ansaätze* transform as

$$\begin{aligned} A_{ij} &\rightarrow \exp[-i\phi(i) - i\phi(j)] A_{ij}, \\ B_{ij} &\rightarrow \exp[+i\phi(i) - i\phi(j)] B_{ij}. \end{aligned} \tag{44}$$

Under this, all the physical observables should remain invariant, but a subset of this, the U(1) transformation keeps the *Ansätze* themselves invariant. The set of the elements of PSGs that are of the kind in Eq. (43) form a group called the invariant gauge group (IGG) [61]. For a honeycomb lattice with both nonzero A_{ij} and B_{ij}, this IGG is simply $\mathbb{Z}_2$ [45]. For the honeycomb lattice, such a PSG classification was found to give two distinct spin-liquid states classified as 0 and π flux states [45]. The spin-liquid states we found from numerical simulations, starting from completely unrestricted *Ansätze*, match with the zero flux states mentioned above.

The symmetries of the *Ansatz* that identifies the nature of the ground state are following [45,56]:

(1) In the spin liquid and the Néel state:

$$\begin{aligned} &A_{11} = A_{12} = A_{13} = \mathcal{A}, \\ &A^u_{21} = A^u_{22} = A^u_{23} = A^v_{21} = A^v_{22} = A^v_{23} = 0, \\ &B_{11} = B_{12} = B_{13} = 0, \\ &B^u_{21} = B^u_{22} = B^u_{23} = B^v_{21} = B^v_{22} = B^v_{23} = \mathcal{B}. \end{aligned} \tag{45}$$

(2) In the VBC state:

$$\begin{aligned} &A_{11} \neq A_{12} = A_{13}, \\ &A^u_{21} \neq A^u_{22} = -A^u_{23}, \\ &A^v_{21} \neq A^v_{22} = -A^v_{23}, \\ &B_{11} \neq B_{12} = B_{13}, \\ &B^u_{21} \neq B^u_{22} = B^u_{23}, \\ &B^v_{21} \neq B^v_{22} = B^v_{23}. \end{aligned} \tag{46}$$

(3) In spiral-ordered state:

$$\begin{aligned} &A_{11} = A_{12} \neq A_{13}, \\ &A^u_{21} \neq A^u_{22} = -A^u_{23}, \\ &A^v_{21} \neq A^v_{22} = -A^v_{23}, \\ &B_{11} = B_{12} \neq B_{13}, \\ &B^u_{21} \neq B^u_{22} = B^u_{23}, \\ &B^v_{21} \neq B^v_{22} = B^v_{23}. \end{aligned} \tag{47}$$

For the CZSL phase:

(1) Real part:

$$\begin{aligned} &A_{11} \neq A_{12} = A_{13}, \\ &A^u_{21} = -A^u_{23} \neq A^u_{23}, A^v_{21} = -A^v_{23} \neq A^v_{22}, \\ &B_{11} \neq B_{12} \neq B_{13}, \\ &B^u_{21} = B^u_{23} \neq B^u_{22}, B^v_{21} = B^v_{23} \neq B^v_{22}. \end{aligned} \tag{48}$$

(2) Imaginary part:

$$\begin{aligned} &A_{11} \neq A_{12} = -A_{13}, \\ &A^u_{21} = A^u_{23} \neq A^u_{22}, A^v_{21} = A^v_{23} \neq A^v_{22}, \\ &B_{11} \neq B_{12} \neq B_{13}, \\ &B^u_{21} = B^u_{23} \neq B^u_{22}, B^v_{21} = B^v_{23} \neq B^v_{22}. \end{aligned} \tag{49}$$

The broken TR symmetry in the CZSL state gives rise to a nonvanishing imaginary part of the mean-field parameters [46,63]. This can be understood in the following way: The

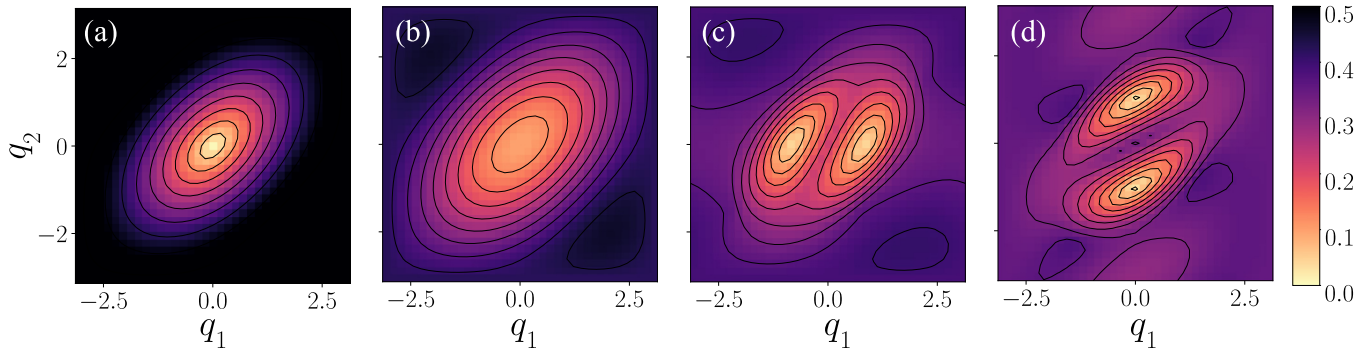

FIG. 3. Momentum dependence of the lowest spinon band for $J_\chi = 0$ corresponding to four different phases: (a) $J_2/J_1 = 0.197$ (Néel phase), (b) $J_2/J_1 = 0.35$ [gapped spin-liquid (GSL) phase], (c) $J_2/J_1 = 0.38$ [valence-bond crystal (VBC) phase], and (d) $J_2/J_1 = 0.43$ (spiral antiferromagnetic phase).

scaler chiral interaction Hamiltonian can be written as Eq. (9). Now, within SBMFT, the expectation values of the loop operators can be written as

$$\langle \hat{B}_{ij}\hat{B}_{jk}\hat{B}_{ki}\rangle \approx B_{ij}B_{jk}B_{ki}. \tag{50}$$

Now it is clear from Eq. (9) that the real-valued mean-field *Ansatz* imposes $\langle \vec{S}_i \cdot (\vec{S}_j \times \vec{S}_k)\rangle = 0$ and does not break the TR symmetry or give rise to a noncoplanar spin configuration. The complex arguments of the loops which are called fluxes break the TR symmetry that invalidates the relation $\Omega_n^z(\vec{k}) = -\Omega_n^z(-\vec{k})$, which is the condition for a nonzero Chern number. Our numerical findings show that, beyond a critical value of J_χ, the *Ansatz* B_2 becomes imaginary, leading to a change in the Chern number which marks a topological phase transition. Additionally, we find that reflection symmetry breaking ($B_{2u}^d \neq B_{2v}^d$) is necessary for a nontrivial topological phase. In our case, $\mathcal{A}$ and $\mathcal{B}$ are both nonzero in numerical findings, so we identify the GSL state as a $\mathbb{Z}_2$ QSL [46], and the topologically nontrivial QSL phase as a CZSL state [63–65].

2. C_3 symmetry-breaking order parameter

In the intermediate spin-disordered region, in the VBC state, the spin-rotational symmetry SU(2) and transnational symmetries are intact, but they may break the C_3-rotational symmetry of the lattice. Following Okumura *et al.* [66], we define a C_3-rotational symmetry-breaking order parameter:

$$\psi_3 = p_1\vec{a}_1 + p_2\vec{a}_2 + p_3\vec{a}_3, \tag{51}$$

with

$$p_i = J_1\left(B_{1i}^2 - A_{1i}^2\right).$$

Here, p_α ($\alpha = 1, 2, 3$) are nothing but the bond energies corresponding to nearest-neighbor bonds $\vec{a}_\alpha$ ($\alpha = 1, 2, 3$). This order parameter is zero if the bond energies remain the same along three different directions.

IV. NUMERICAL RESULTS

Without the application of the scalar chiral term (i.e., keeping $J_\chi = 0$), numerically, we find, for $J_2 \leqslant 0.22$, the ground state is gapless (defined as a gap $< 1/N_s$), with Néel order, and spiral magnetic order is also found for larger values of $J_2 > 0.4$. A gapped phase is found in the intermediate range $0.22 < J_2 < 0.4$ between the Néel and spiral orders. Within a range of $0.37 \leqslant J_2 < 0.4$, we find the staggered VBC phase, with the nonzero C_3 symmetry-breaking order parameter defined in Eq. (51). We call the rest of the gapped region a GSL state. These findings match with previous studies [56,67].

In Fig. 3, we show the lower spinon (particle) bands, without the application of J_χ in all four different phases. The Brillouin zone is from $-\pi$ to π in both momentums, measured along the directions along the reciprocal translation vectors. The dispersion in the Néel ordered phase shows the characteristic minima (with gap $< 1/N$) at the $(0, 0)$ momentum, which shifts away from this point in the case of the spiral ordered state. The spectra for the GSL and VBC states are gapped with different positions of minima in the band. The gap in the spectrum for different phases is shown in the Fig. 4, where we also show, in the inset of the same figure, the sudden rise in the ψ_3 order parameter in the VBC state. In Appendix B, we have investigated the system size dependence of the gap of the lower spinon band for different values of J_2.

Within the GSL state, as J_χ is increased, we find, beyond a certain value of J_χ, either the state becomes gapless with Néel

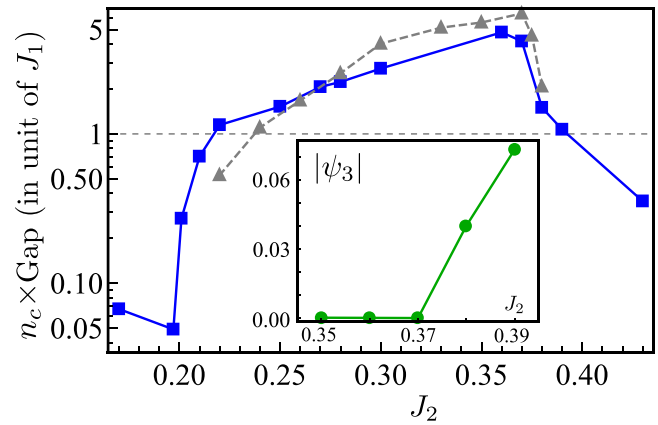

FIG. 4. Blue curve indicates the gap in the excitation spectrum as a function of J_2, with $J_\chi = 0$, distinguishing gapped and gapless (defined as when the gap is $< 1/N_s$, with $N_s = 36$ in our case) phases. The gray curve corresponds to the same plot with a different system size $N_s = 48$. Inset: The C_3 symmetry-breaking order parameter ψ_3, defined in Eq. (51), becomes nonzero in the small window of J_2, when we expect the valence-bond crystal (VBC) ground state.

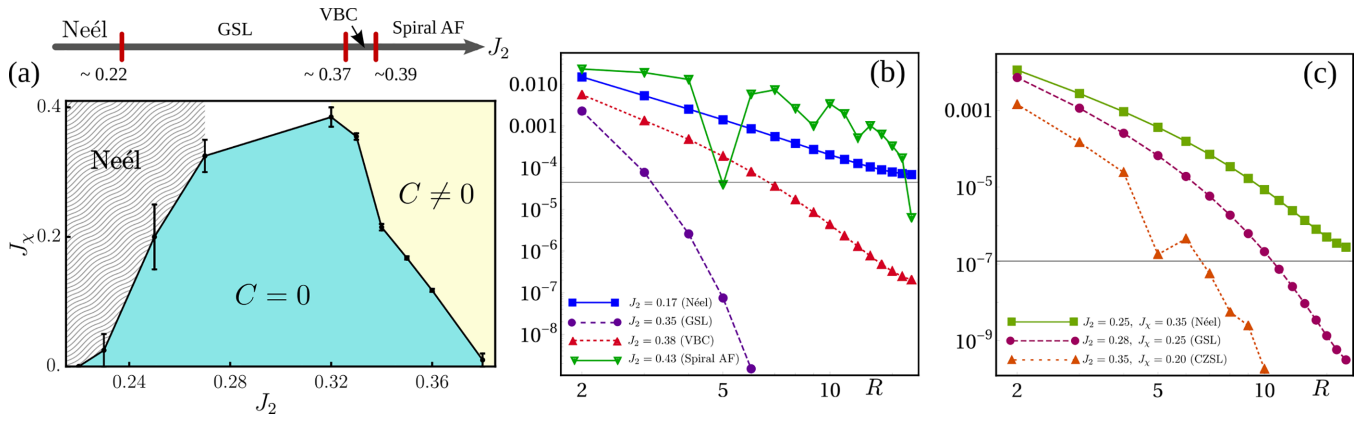

FIG. 5. (a) Phase diagram of J_1-J_2-J_χ Heisenberg model on the honeycomb lattice. Above: The phase diagram without the spin-chiral term (i.e., $J_\chi = 0$). Below: The phase diagram with the scalar spin-chiral term, where a gapped chiral $\mathbb{Z}_2$ spin-liquid phase (CZSL) emerges with nonvanishing Chern number of the spinon bands. We set $J_1 = 1$ as our scale of energy. We identify the various phase with the symmetry of the order parameters (see Sec. III), the gap in the spectrum, as well as how the spin-spin correlation function decays. (b) and (c) show the spin-spin correlation functions $|\langle\vec{S}_0 \cdot \vec{S}_R\rangle/\langle\vec{S}_0 \cdot \vec{S}_0\rangle|$, as a function of R (along $\hat{e}_2$) in a log-log scale. (b) shows such correlations without the chiral spin term J_χ, whereas in (c), we show the same with $J_\chi \neq 0$, for various phases. It is evident that the correlation decays much faster in gapped spin-liquid (GSL), CZSL, and valence-bond crystal (VBC) phases, whereas the decay is slower for the case of gapless states.

ordering, or the bands acquire a nonzero Chern number, which we identify as a CZSL state. It is important to note that, in the CZSL state, spinon bands remain gapped but with increasing perturbation (J_χ); the particle bands themselves come closer, leading to topological phase transition for a critical J_χ. If we start instead from a VBC state, for a critical perturbation, we also observe a topological transition in the spinon bands (the ground state remains gapped).

In Fig. 5(a), we show the full phase diagram including J_χ, which leads to a possible CZSL state, characterized by a nonzero Chern number of the excitation bands. We also show the static spin-spin correlation, defined in the Sec. II D, in Figs. 5(b) and 5(c) for the phases without J_χ and with J_χ, respectively. From these logarithmic scaled plots, it is evident that the spin-spin correlation $|\langle\vec{S}_0 \cdot \vec{S}_R\rangle|$ decays at a much faster rate, as a function of the distance R, in the GSL, CZSL, and VBC states than magnetically ordered states, which is expected.

With increasing J_χ, at a critical J_χ, there is a topological transition to a nonzero Chern number (C) state, which can also be seen from the Berry curvatures of the spinon bands. When $C \neq 0$, the symmetry of the Berry curvature is lost, i.e., $\Omega(\vec{q}) \neq \Omega(-\vec{q})$. The plot of the Berry curvature is shown in Fig. 6, before and after such a topological transition.

1. Nature of Chern transitions within CZSL

We have also studied a number of topological transitions with increasing J_χ, in Fig. 7, where the system undergoes a series of topological transitions with different Chern numbers. In Fig. 7(a), we show all Chern transitions for various representative values of J_2 corresponding to different phases of the system as a function of J_χ. Chern transitions imply interband gap closing, which we illustrate through FIig. 7(b) for a particular value of $J_2 = 0.35$. We have identified all the transitions where the interband gap attains a minimum value

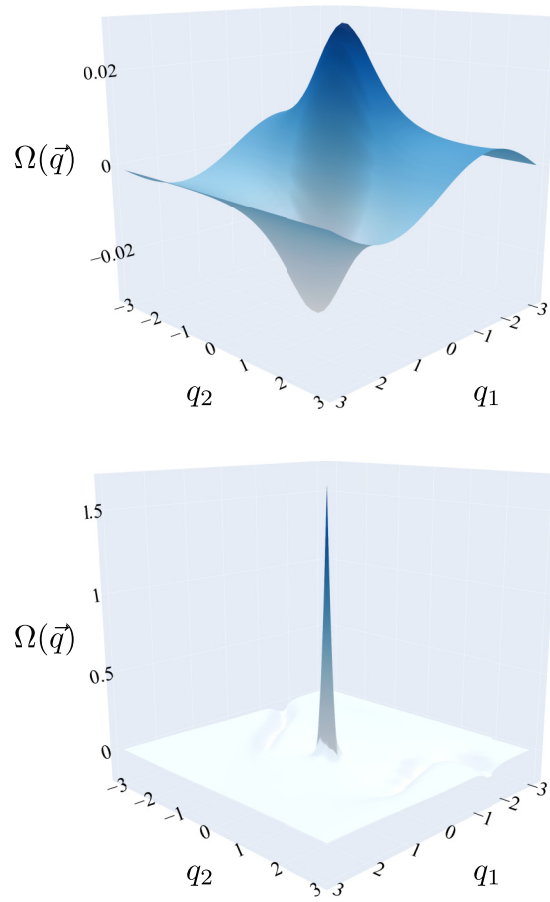

FIG. 6. Plot of the momentum resolved Berry curvature (Ω) of the lower spinon band for $J_2 = 0.35$; with $J_\chi = 0.15$ (top), which is before the transition to chiral $\mathbb{Z}_2$ (CZSL), and $J_\chi = 0.17$ (bottom), after the transition to CZSL. The value of Ω is shown in the units of $1/\delta q_1 \delta q_2$, where δq_i is the momentum-grid separation for the ith direction.

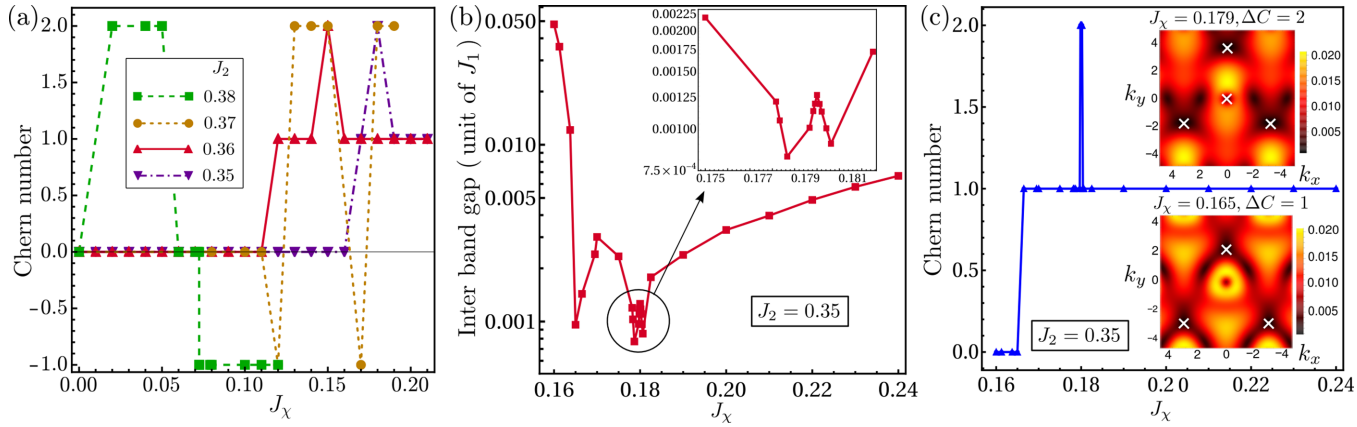

FIG. 7. (a) Chern transitions (upper band) with respect to J_χ for a few values of J_2. For $J_2 = 0.38$ and 0.37, there are transitions from $C = 2$ to -1. Plot of (b) gap and (c) Chern number with respect to J_χ for $J_2 = 0.35$ corroborates transitions from (a). Three Chern transitions are accompanied by three band touchings. The inset in (c) shows the gap-closing points in the Brillouin zone.

(i.e., a gap closing) as a function of J_χ. To gain more insight, we identify the gap closing points in each transition in the full Brillouin zone, which differ quantitatively [see Fig. 7(c)]. We observe that, in the $\Delta C = 1$ transition, there is only one band touching point, whereas for the $\Delta C = 2$ transition, there are two band touching points.

2. Thermal Hall effect

Finally, in Fig. 8, we show the thermal Hall coefficient in the states with $C \neq 0$, which peaks to an appreciable value at a temperature equal to the gap in the lower spinon band. Due to the preserved symmetry of the Berry curvature, the Hall coefficient is vanishingly small in the case of the state with $C = 0$. In Appendix C, we have also briefly studied the effect of a nonzero Zeeman field on the thermal Hall coefficient within the SBMFT formalism.

V. DISCUSSION

In conclusion, we investigated, within SBMFT, the phase transition from a gapped $\mathbb{Z}_2$ QSL, in a J_1-J_2 Heisenberg spin-$\frac{1}{2}$ system in a honeycomb lattice, to a CZSL phase under the presence of a TR symmetry-breaking scalar-chiral interaction (with amplitude J_χ). The CZSL state is characterized by TR broken mean-field parameters, nontrivial Chern bands for excitations, and lack of long-range magnetic order. In this CZSL phase, we find a nontrivial Chern number of the spinon bands leads to a large thermal Hall coefficient.

The study is limited by the finite-sized effects in the spectrum, and a comparison with larger system size is left for future study. Similarly, the topological invariant computation can be erroneous in situations when the gap between the spinon bands is small. We explored series of topological transitions with increase of the value of J_χ, but further exploration of the same and effects of possible protected edge modes of spinons is left for future study.

Possible materials for QSL states in Mott insulating states in a honeycomb lattice, where the physics we explored can be possible to observe, include inorganic materials such as $Na_2Co_2TeO_6$ [68], $BaM_2(XO_4)_2$ (with $X = As$) [69], $Bi_3Mn_4O_{12}(NO_3)$ [70], and $In_3Cu_2VO_9$ [71], where the magnitudes of spin vary from $S = \frac{1}{2}$ in $BaM_2(XO_4)_2$ for $M = Co$ to $S = 1$ for $M = Ni$ (with $X = As$) and $S = \frac{3}{2}$ in $Bi_3Mn_4O_{12}(NO_3)$. Spin-orbit coupled materials, such as $In_3Cu_2VO_9$, have also recently been explored [71], where the Cu ions form a honeycomb structure with spin-$\frac{1}{2}$ local mo-

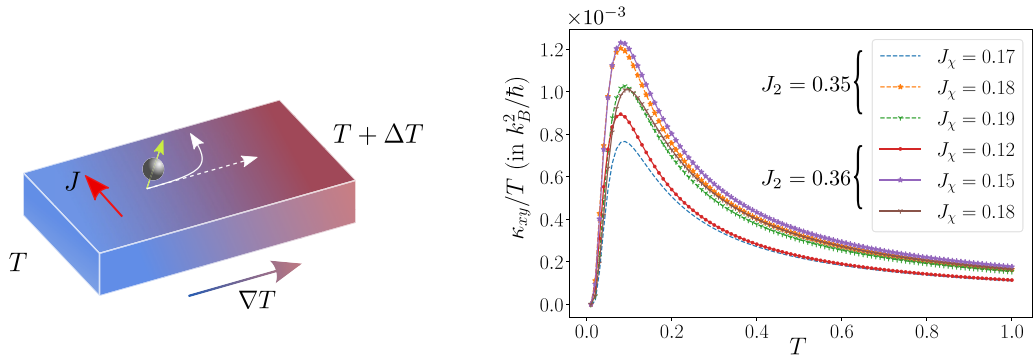

FIG. 8. Left: Schematic picture of the setup where thermal Hall current carried by spinons in the presence of a longitudinal magnetic field, where the role of the magnetic field is played by the scalar chiral coupling in our system. Right: Thermal Hall coefficient (κ_{xy}) as a function of the temperature for the states with $C \neq 0$. A critical T for the nonzero κ_{xy} reflects the fact that the spinon bands are gapped. In the states with $C = 0$, the Hall coefficient is zero, in comparison.

ments, which are also possible candidates. Another possible avenue of realizing spin systems is cold-atomic experiments where strongly correlated systems have been explored in recent times [72–75].

ACKNOWLEDGMENTS

R.M. is grateful for useful communication with S. Chatterjee (University of California, Berkeley), A. Ralko (Néel Institute, CNRS Grenoble), and J. Merino (Universidad Autónoma de Madrid). A.K. acknowledges support from the Government of India: Science and Engineering Research Board via Sanction No. ECR/2018/001443 and CRG/2020/001803, Department of Atomic Energy via Sanction No. 58/20/15/2019-BRNS, as well as Ministry of Human Resource Development via Sanction No. SPARC/2018-2019/P538/SL. R.M. acknowledges the Council of Scientific and Industrial Research (Government of India) for financial support. R.K. acknowledges funding under the Prime Minister's Research Fellows scheme (Government of India). We also acknowledge the use of the high-performance computing facility at Indian Institute of Technology Kanpur.

APPENDIX A: BERRY CURVATURE AND U(1)-LINK VARIABLE

Here, we briefly summarize the method of Berry-curvature computation, especially for the bosonic case, following Refs. [76,77]. We first consider a two-dimensional fermionic system with the Brillouin zone defined by $0 \leqslant q_\mu < 2\pi/a_\mu$ ($\mu = 1, 2$ with some integer a_μ). As the Hamiltonian $H(q_1, q_2)$ is periodic in both directions, $H(q_1, q_2) = H(q_1 + 2\pi/a_1, q_2) = H(q_1, q_2 + 2\pi/a_2)$.

The Berry connection $A_\mu(q)$ ($\mu = 1, 2$) and the corresponding field strength $F_{12}(q)$, for the nth band, are given by

$$A^n_\mu(q) = \langle n(q)|\, \partial_\mu\, |n(q)\rangle\,, \tag{A1}$$

$$F^n_{12}(k) = \partial_1 A^n_2(q) - \partial_2 A^n_1(q), \tag{A2}$$

where $|n(q)\rangle$ is a normalized wave function of the nth Bloch band such that

$$H(q)\,|n(q)\rangle = E_n(q)\,|n(q)\rangle\,. \tag{A3}$$

In the expression above, the derivative ∂_μ stands for ∂_{q_μ}. We assume that there is no degeneracy for the nth state.

The Berry curvature is computed as follows. First, we discretize the Brillouin zone as follows:

$$q_l = (q_{j_1}, q_{j_2}), \qquad q_{j_\mu} = \frac{2\pi\, j_\mu}{a_\mu N_\mu}, \quad (j_\mu = 0, \ldots, N_\mu - 1), \tag{A4}$$

with discretization $\delta q_\mu = 2\pi/a_\mu N_\mu$, where a_μ is the lattice spacing in $\hat{\mu}$th direction. It is also assumed that the state $|n(\vec{q})\rangle$ is periodic on the lattice:

$$|n(\vec{q} + N_\mu \hat{\mu})\rangle = |n(k_l)\rangle\,, \tag{A5}$$

where $\hat{\mu}$ is a vector in the direction μ with magnitude $2\pi/(a_\mu N_\mu)$. We define the U_1-link variable for the nth band as

$$U^n_{\hat{\mu}}(\vec{q}) \equiv \frac{\langle n(\vec{q})|n(\vec{q} + \hat{\mu})\rangle}{N^n_{\hat{\mu}}(\vec{q})}, \tag{A6}$$

where

$$N^n_{\hat{\mu}}(\vec{q}) \equiv |\langle n(\vec{q})|n(\vec{q} + \hat{\mu})\rangle|. \tag{A7}$$

The link variables are well defined if $N^n_{\hat{\mu}}(\vec{q}_l) \neq 0$, which can always be assumed to be the case (one can avoid a singular point by infinitesimal shift of the lattice). The field strength is then numerically approximated by

$$F^n_{12}(\vec{q})\delta q_1 \delta q_2 \approx \log_e U^n_1(\vec{q}) U^n_2(\vec{q} + \hat{1}) \times U^n_1(\vec{q} + \hat{2})^{-1} U^n_2(\vec{q})^{-1}, \tag{A8}$$

with

$$-\pi < \frac{1}{i} F^n_{12}(\vec{q})\delta q_1 \delta q_2 \leqslant \pi\,. \tag{A9}$$

Field strength is defined within the principle branch of the logarithm specified in Eq. (A8). It should also be noted that field strength is gauge invariant. The Berry curvature is expressed in terms of the field strength as

$$\Omega^n(\vec{q}) = -iF_{12}(\vec{q}). \tag{A10}$$

Finally, the Chern number on the lattice corresponding to the nth band is defined as

$$C_n \equiv \frac{1}{2\pi i} \sum_{\vec{q}} F_{12}(\vec{q})\delta q_1 \delta q_2. \tag{A11}$$

For the bosonic case

To accommodate the commutation relations among the bosonic operators, the generalized eigenvalue equation in the case of a bosonic Hamiltonian M is written as

$$M(q)\,|n(\vec{q})\rangle = E(\vec{q})\rho_3\,|n(\vec{q})\rangle\,. \tag{A12}$$

As a consequence, the inner product in the U(1)-link variable has the form [77]:

$$U_{\hat{\mu}}(\vec{q}) \equiv \frac{\langle n(\vec{q})|\,\rho_3\,|n(\vec{q} + \hat{\mu})\rangle}{N_{\hat{\mu}}(\vec{q})}, \tag{A13}$$

where

$$N_{\hat{\mu}}(\vec{q}) \equiv |\,\langle n(\vec{q})|\,\rho_3\,|n(\vec{q} + \hat{\mu})\rangle\,|. \tag{A14}$$

Here, $E(\vec{q})$ has eigenvalues of the form:

$$(\epsilon_{\vec{q},\uparrow}, \epsilon_{\vec{q},\downarrow}, -\epsilon_{\vec{q},\uparrow}, -\epsilon_{\vec{q},\downarrow}). \tag{A15}$$

For particle/hole bands, the eigenvector $|n(\vec{q})\rangle$ is normalized as follows:

$$\langle n^{\text{particle}}(\vec{q})|\,\rho_3|n^{\text{particle}}(\vec{q})\rangle = 1, \tag{A16}$$

$$\langle n^{\text{hole}}(\vec{q})|\,\rho_3|n^{\text{hole}}(\vec{q})\rangle = -1. \tag{A17}$$

APPENDIX B: SYSTEM SIZE DEPENDENCE OF THE GAP

We have studied how the gap (Δ) of the lowest spinon band changes with increasing system size (n_c, where n_c is the total number of unit cells). Our findings show that, with increasing n_c, the system persists to have a constant gap in the

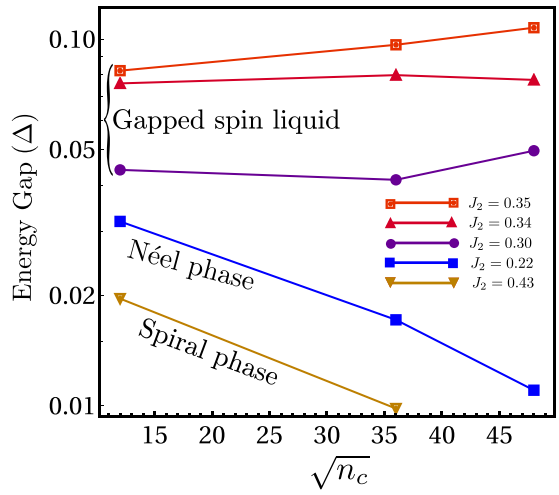

FIG. 9. This figure shows the dependence of system size ($\sqrt{n_c}$) on the energy gap (Δ) of the lowest spinon band. For the gapless phase, Δ decreases with increasing system size, whereas in the gapped spin-liquid phase, Δ converges to a finite value. Extrapolation of this leads to vanishing of Δ for Néel and spiral phases in the thermodynamic limit.

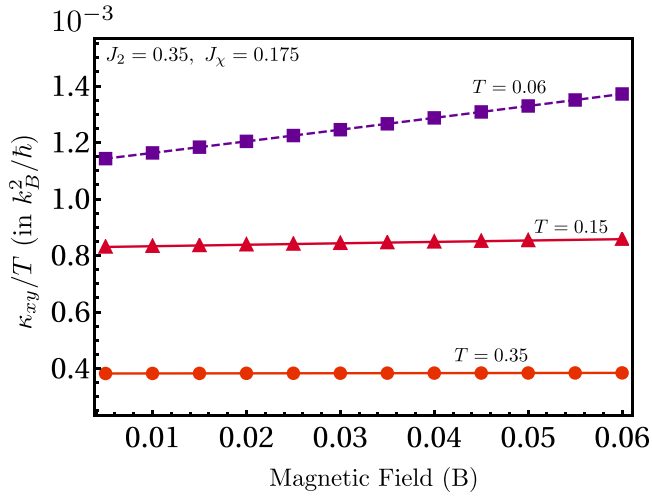

FIG. 10. This plot shows the magnetic field dependence of the thermal Hall conductivity for different values of the temperature. For large temperature, the Hall conductivity is approximately linear, whereas it becomes weakly nonlinear for the low-temperature regime.

GSL phase, whereas for gapless phases, such as the Néel and spiral phases, the gap monotonically decreases. The findings are summarized in Fig. 9.

APPENDIX C: EFFECT OF NONZERO ZEEMAN FIELD

In the presence of a nonzero out-of-plane magnetic field, the spin-rotation invariance of our Hamiltonian is broken, and the Zeeman term of the Hamiltonian reads

$$H_Z = -B_z \sum_i S_i^z = \frac{B_z}{2} \sum_{i,\sigma,\sigma'} b_{i,\sigma}^\dagger (\sigma_z)_{\sigma,\sigma'} b_{i,\sigma'}. \tag{C1}$$

In the dynamical matrix, this Zeeman term is proportional to an identity matrix, rendering the eigenstates of the spinon bands intact [34]. As a result, the Berry curvature remains the same. As the $T_{\vec{q}}$ matrix is invariant, the *Ansätze* are also invariant under the application of the magnetic field. In Schwinger-boson theory, the *Ansätze* we take are SU(2) symmetric, so the magnetic field does not change the wave functions. In terms of the Schwinger-boson operators, the Zeeman term can be recast into the form:

$$-\frac{\mu_B B}{2} \sum_i \langle b_{i,\uparrow}^\dagger b_{i,\uparrow} \rangle - \langle b_{i,\downarrow}^\dagger b_{i,\downarrow} \rangle . \tag{C2}$$

Effectively, the magnetic field leads to different chemical potentials for the $\uparrow$ and $\downarrow$ spin flavors of Schwinger bosons. This breaks the up-down spin symmetry, i.e., the dispersion of up and down spins becomes different, $e^w_{\vec{q},\uparrow} \neq e^w_{\vec{q},\downarrow}$. After diagonalization, the mean-field Hamiltonian takes the form:

$$H(B) = \sum_{\vec{q},\sigma,w} \epsilon^w_{\vec{q},\sigma} \left[\gamma^\dagger_{\vec{q},\sigma,w} \gamma_{\vec{q},\sigma,w} + \frac{1}{2} \right] + \text{constant terms}. \tag{C3}$$

We have studied the effect of a nonzero Zeeman field on the thermal Hall conductivity of the particle bands in the CZSL phase for different values of temperature. Figure 10 presents a summary of the results.

This discussion is limited for the case when there is no Bose-Einstein condensation, which can happen in the presence of a large magnetic field. In that case, the gap of one of the bands may go to zero, leading to a magnetic ordering and Goldstone modes.

[1] C. Broholm, R. J. Cava, S. A. Kivelson, D. G. Nocera, M. R. Norman, and T. Senthil, Quantum spin liquids, Science **367**, eaay0668 (2020).
[2] L. Balents, Spin liquids in frustrated magnets, Nature (London) **464**, 199 (2010).
[3] J. Wen, S.-L. Yu, S. Li, W. Yu, and J.-X. Li, Experimental identification of quantum spin liquids, npj Quantum Mater. **4**, 12 (2019).
[4] P. W. Anderson, The resonating valence bond state in La_2CuO_4 and superconductivity, Science **235**, 1196 (1987).
[5] A. Kitaev, Anyons in an exactly solved model and beyond, Ann. Phys. **321**, 2 (2006).
[6] G. Jackeli and G. Khaliullin, Mott Insulators in the Strong Spin-Orbit Coupling Limit: From Heisenberg to a Quantum Compass and Kitaev Models, Phys. Rev. Lett. **102**, 017205 (2009).
[7] J. G. Rau, E. K.-H. Lee, and H.-Y. Kee, Spin-orbit physics giving rise to novel phases in correlated systems: Iridates and related materials, Annu. Rev. Condens. Matter Phys. **7**, 195 (2016).

[8] S. M. Winter, Y. Li, H. O. Jeschke, and R. Valentí, Challenges in design of Kitaev materials: Magnetic interactions from competing energy scales, Phys. Rev. B **93**, 214431 (2016).

[9] N. Read and S. Sachdev, Valence-Bond and Spin-Peierls Ground States of Low-Dimensional Quantum Antiferromagnets, Phys. Rev. Lett. **62**, 1694 (1989).

[10] N. Read and S. Sachdev, Large-N Expansion for Frustrated Quantum Antiferromagnets, Phys. Rev. Lett. **66**, 1773 (1991).

[11] B. K. Clark, D. A. Abanin, and S. L. Sondhi, Nature of the Spin Liquid State of the Hubbard Model on a Honeycomb Lattice, Phys. Rev. Lett. **107**, 087204 (2011).

[12] Z. Zhu, D. A. Huse, and S. R. White, Weak Plaquette Valence Bond Order in the $S = \frac{1}{2}$ Honeycomb J_1-J_2 Heisenberg Model, Phys. Rev. Lett. **110**, 127205 (2013).

[13] R. F. Bishop, P. H. Y. Li, D. J. J. Farnell, and C. E. Campbell, The frustrated Heisenberg antiferromagnet on the honeycomb lattice: J_1-J_2 model, J. Phys.: Condens. Matter **24**, 236002 (2012).

[14] J. Liu, Y.-M. Quan, H. Q. Lin, and L.-J. Zou, Topologically different spin disorder phases of the J_1-J_2 Heisenberg model on the honeycomb lattice, Phys. E **120**, 114037 (2020).

[15] A. F. Albuquerque, D. Schwandt, B. Hetényi, S. Capponi, M. Mambrini, and A. M. Läuchli, Phase diagram of a frustrated quantum antiferromagnet on the honeycomb lattice: Magnetic order versus valence-bond crystal formation, Phys. Rev. B **84**, 024406 (2011).

[16] F. Ferrari, S. Bieri, and F. Becca, Competition between spin liquids and valence-bond order in the frustrated spin-$\frac{1}{2}$ Heisenberg model on the honeycomb lattice, Phys. Rev. B **96**, 104401 (2017).

[17] R. Ganesh, J. van den Brink, and S. Nishimoto, Deconfined Criticality in the Frustrated Heisenberg Honeycomb Antiferromagnet, Phys. Rev. Lett. **110**, 127203 (2013).

[18] F. Mezzacapo and M. Boninsegni, Ground-state phase diagram of the quantum J_1-J_2 model on the honeycomb lattice, Phys. Rev. B **85**, 060402(R) (2012).

[19] K. Yang, S.-H. Phark, Y. Bae, T. Esat, P. Willke, A. Ardavan, A. J. Heinrich, and C. P. Lutz, Probing resonating valence bond states in artificial quantum magnets, Nat. Commun. **12**, 1 (2021).

[20] S.-S. Gong, W. Zhu, and D. Sheng, Emergent chiral spin liquid: Fractional quantum Hall effect in a kagome Heisenberg model, Sci. Rep. **4**, 6317 (2014).

[21] B. Bauer, L. Cincio, B. P. Keller, M. Dolfi, G. Vidal, S. Trebst, and A. W. Ludwig, Chiral spin liquid and emergent anyons in a kagome lattice Mott insulator, Nat. Commun. **5**, 5137 (2014).

[22] A. Wietek, A. Sterdyniak, and A. M. Läuchli, Nature of chiral spin liquids on the kagome lattice, Phys. Rev. B **92**, 125122 (2015).

[23] Y.-C. He, D. N. Sheng, and Y. Chen, Chiral Spin Liquid in a Frustrated Anisotropic Kagome Heisenberg Model, Phys. Rev. Lett. **112**, 137202 (2014).

[24] W. Zhu, S. S. Gong, and D. N. Sheng, Chiral and critical spin liquids in a spin-$\frac{1}{2}$ kagome antiferromagnet, Phys. Rev. B **92**, 014424 (2015).

[25] L. Messio, S. Bieri, C. Lhuillier, and B. Bernu, Chiral Spin Liquid on a Kagome Antiferromagnet Induced by the Dzyaloshinskii-Moriya Interaction, Phys. Rev. Lett. **118**, 267201 (2017).

[26] R. G. Pereira and S. Bieri, Gapless chiral spin liquid from coupled chains on the kagome lattice, SciPost Phys. **4**, 004 (2018).

[27] P. Nataf, M. Lajkó, A. Wietek, K. Penc, F. Mila, and A. M. Läuchli, Chiral Spin Liquids in Triangular-Lattice SU(N) Fermionic Mott Insulators with Artificial Gauge Fields, Phys. Rev. Lett. **117**, 167202 (2016).

[28] A. Wietek and A. M. Läuchli, Chiral spin liquid and quantum criticality in extended $S = \frac{1}{2}$ Heisenberg models on the triangular lattice, Phys. Rev. B **95**, 035141 (2017).

[29] S.-S. Gong, W. Zhu, J.-X. Zhu, D. N. Sheng, and K. Yang, Global phase diagram and quantum spin liquids in a spin-$\frac{1}{2}$ triangular antiferromagnet, Phys. Rev. B **96**, 075116 (2017).

[30] S.-S. Gong, W. Zheng, M. Lee, Y.-M. Lu, and D. N. Sheng, Chiral spin liquid with spinon Fermi surfaces in the spin-$\frac{1}{2}$ triangular Heisenberg model, Phys. Rev. B **100**, 241111(R) (2019).

[31] J.-Y. Chen, L. Vanderstraeten, S. Capponi, and D. Poilblanc, Non-Abelian chiral spin liquid in a quantum antiferromagnet revealed by an iPEPS study, Phys. Rev. B **98**, 184409 (2018).

[32] C. Hickey, L. Cincio, Z. Papić, and A. Paramekanti, Haldane-Hubbard Mott Insulator: From Tetrahedral Spin Crystal to Chiral Spin Liquid, Phys. Rev. Lett. **116**, 137202 (2016).

[33] Y. Gao, X.-P. Yao, and G. Chen, Topological phase transition and nontrivial thermal Hall signatures in honeycomb lattice magnets, Phys. Rev. Res. **2**, 043071 (2020).

[34] R. Samajdar, S. Chatterjee, S. Sachdev, and M. S. Scheurer, Thermal Hall effect in square-lattice spin liquids: A Schwinger boson mean-field study, Phys. Rev. B **99**, 165126 (2019).

[35] S. Katsura, T. Ide, and T. Morita, The ground states of the classical Heisenberg and planar models on the triangular and plane hexagonal lattices, J. Stat. Phys. **42**, 381 (1986).

[36] E. Rastelli, A. Tassi, and L. Reatto, Non-simple magnetic order for simple Hamiltonians, Physica B+C **97**, 1 (1979).

[37] J. Fouet, P. Sindzingre, and C. Lhuillier, An investigation of the quantum J_1-J_2-J_3 model on the honeycomb lattice, Eur. Phys. J. B **20**, 241 (2001).

[38] A. Mulder, R. Ganesh, L. Capriotti, and A. Paramekanti, Spiral order by disorder and lattice nematic order in a frustrated Heisenberg antiferromagnet on the honeycomb lattice, Phys. Rev. B **81**, 214419 (2010).

[39] R. Ganesh, D. N. Sheng, Y.-J. Kim, and A. Paramekanti, Quantum paramagnetic ground states on the honeycomb lattice and field-induced Néel order, Phys. Rev. B **83**, 144414 (2011).

[40] T. Einarsson and H. Johannesson, Effective-action approach to the frustrated Heisenberg antiferromagnet in two dimensions, Phys. Rev. B **43**, 5867 (1991).

[41] H. Mosadeq, F. Shahbazi, and S. Jafari, Plaquette valence bond ordering in a J_1-J_2 Heisenberg antiferromagnet on a honeycomb lattice, J. Phys.: Condens. Matter **23**, 226006 (2011).

[42] J. Reuther, D. A. Abanin, and R. Thomale, Magnetic order and paramagnetic phases in the quantum J_1-J_2-J_3 honeycomb model, Phys. Rev. B **84**, 014417 (2011).

[43] G. Kotliar and J. Liu, Superexchange mechanism and d-wave superconductivity, Phys. Rev. B **38**, 5142 (1988).

[44] X.-G. Wen, Quantum orders and symmetric spin liquids, Phys. Rev. B **65**, 165113 (2002).

[45] F. Wang, Schwinger boson mean field theories of spin liquid states on a honeycomb lattice: Projective symmetry group analysis and critical field theory, Phys. Rev. B **82**, 024419 (2010).

[46] F. Wang and A. Vishwanath, Spin-liquid states on the triangular and kagomé lattices: A projective-symmetry-group analysis of Schwinger boson states, Phys. Rev. B **74**, 174423 (2006).

[47] C. Xu and S. Sachdev, Majorana Liquids: The Complete Fractionalization of the Electron, Phys. Rev. Lett. **105**, 057201 (2010).

[48] S. Florens and A. Georges, Slave-rotor mean-field theories of strongly correlated systems and the Mott transition in finite dimensions, Phys. Rev. B **70**, 035114 (2004).

[49] M. Hermele, SU(2) gauge theory of the Hubbard model and application to the honeycomb lattice, Phys. Rev. B **76**, 035125 (2007).

[50] Y.-M. Lu and Y. Ran, $\mathbb{Z}_2$ spin liquid and chiral antiferromagnetic phase in the Hubbard model on a honeycomb lattice, Phys. Rev. B **84**, 024420 (2011).

[51] A. H. MacDonald, S. M. Girvin, and D. Yoshioka, $\frac{t}{U}$ expansion for the Hubbard model, Phys. Rev. B **37**, 9753 (1988).

[52] Y. Huang, X.-Y. Dong, D. N. Sheng, and C. S. Ting, Quantum phase diagram and chiral spin liquid in the extended spin-$\frac{1}{2}$ honeycomb *xy* model, Phys. Rev. B **103**, L041108 (2021).

[53] O. I. Motrunich, Orbital magnetic field effects in spin liquid with spinon fermi sea: Possible application to κ-$(ET)_2Cu_2(CN)_3$, Phys. Rev. B **73**, 155115 (2006).

[54] D. Sen and R. Chitra, Large-U limit of a hubbard model in a magnetic field: Chiral spin interactions and paramagnetism, Phys. Rev. B **51**, 1922 (1995).

[55] A. Auerbach, *Interacting Electrons and Quantum Magnetism* (Springer-Verlag, New York, 1994).

[56] J. Merino and A. Ralko, Role of quantum fluctuations on spin liquids and ordered phases in the Heisenberg model on the honeycomb lattice, Phys. Rev. B **97**, 205112 (2018).

[57] J. Colpa, Diagonalization of the quadratic boson Hamiltonian, Physica A **93**, 327 (1978).

[58] M.-w. Xiao, Theory of transformation for the diagonalization of quadratic Hamiltonians, arXiv:0908.0787.

[59] D.-V. Bauer and J. O. Fjærestad, Schwinger-boson mean-field study of the J_1-J_2 Heisenberg quantum antiferromagnet on the triangular lattice, Phys. Rev. B **96**, 165141 (2017).

[60] R. Shindou, R. Matsumoto, S. Murakami, and J.-i. Ohe, Topological chiral magnonic edge mode in a magnonic crystal, Phys. Rev. B **87**, 174427 (2013).

[61] X.-G. Wen, Quantum order: A quantum entanglement of many particles, Phys. Lett. A **300**, 175 (2002).

[62] Y. Zhou and X.-G. Wen, Quantum orders and spin liquids inCs_2CuCl_4, arXiv:cond-mat/0210662.

[63] L. Messio, C. Lhuillier, and G. Misguich, Time reversal symmetry breaking chiral spin liquids: Projective symmetry group approach of bosonic mean-field theories, Phys. Rev. B **87**, 125127 (2013).

[64] B. Schneider, J. C. Halimeh, and M. Punk, Projective symmetry group classification of chiral $\mathbb{Z}_2$ spin liquids on the pyrochlore lattice: Application to the spin-$\frac{1}{2}$ XXZ Heisenberg model, Phys. Rev. B **105**, 125122 (2022).

[65] S. Bieri, C. Lhuillier, and L. Messio, Projective symmetry group classification of chiral spin liquids, Phys. Rev. B **93**, 094437 (2016).

[66] S. Okumura, H. Kawamura, T. Okubo, and Y. Motome, Novel spin-liquid states in the frustrated heisenberg antiferromagnet on the honeycomb lattice, J. Phys. Soc. Jpn. **79**, 114705 (2010).

[67] H. Zhang and C. A. Lamas, Exotic disordered phases in the quantum J_1-J_2 model on the honeycomb lattice, Phys. Rev. B **87**, 024415 (2013).

[68] E. Lefrançois, M. Songvilay, J. Robert, G. Nataf, E. Jordan, L. Chaix, C. V. Colin, P. Lejay, A. Hadj-Azzem, R. Ballou *et al.*, Magnetic properties of the honeycomb oxide$Na_2Co_2TeO_6$, Phys. Rev. B **94**, 214416 (2016).

[69] N. Martin, L.-P. Regnault, and S. Klimko, Neutron larmor diffraction study of the $BaM_2(XO_4)_2$ (M = Co, Ni; X = As, P) compounds, J. Phys.: Conf. Ser. **340**, 012012 (2012).

[70] O. Smirnova, M. Azuma, N. Kumada, Y. Kusano, M. Matsuda, Y. Shimakawa, T. Takei, Y. Yonesaki, and N. Kinomura, Synthesis, crystal structure, and magnetic properties of $Bi_3Mn_4O_{12}(NO_3)$ oxynitrate comprising $S = \frac{3}{2}$ honeycomb lattice, J. Am. Chem. Soc. **131**, 8313 (2009).

[71] Y. J. Yan, Z. Y. Li, T. Zhang, X. G. Luo, G. J. Ye, Z. J. Xiang, P. Cheng, L. J. Zou, and X. H. Chen, Magnetic properties of the doped spin-$\frac{1}{2}$ honeycomb-lattice compound $In_3Cu_2VO_9$, Phys. Rev. B **85**, 085102 (2012).

[72] P. N. Jepsen, J. Amato-Grill, I. Dimitrova, W. W. Ho, E. Demler, and W. Ketterle, Spin transport in a tunable Heisenberg model realized with ultracold atoms, Nature (London) **588**, 403 (2020).

[73] N. Goldman, J. C. Budich, and P. Zoller, Topological quantum matter with ultracold gases in optical lattices, Nat. Phys. **12**, 639 (2016).

[74] M. Aidelsburger, M. Lohse, C. Schweizer, M. Atala, J. T. Barreiro, S. Nascimbène, N. Cooper, I. Bloch, and N. Goldman, Measuring the Chern number of Hofstadter bands with ultracold bosonic atoms, Nat. Phys. **11**, 162 (2015).

[75] S. Ebadi, T. T. Wang, H. Levine, A. Keesling, G. Semeghini, A. Omran, D. Bluvstein, R. Samajdar, H. Pichler, W. W. Ho *et al.*, Quantum phases of matter on a 256-atom programmable quantum simulator, Nature (London) **595**, 227 (2021).

[76] T. Fukui, Y. Hatsugai, and H. Suzuki, Chern numbers in discretized Brillouin zone: Efficient method of computing (spin) Hall conductances, J. Phys. Soc. Jpn. **74**, 1674 (2005).

[77] P. Wang, L. Lu, and K. Bertoldi, Topological Phononic Crystals with One-Way Elastic Edge Waves, Phys. Rev. Lett. **115**, 104302 (2015).